UC San Diego
UC San Diego Previously Published Works

Title

Modeling long-period noise in kinematic GPS applications

Authors

Borsa, Adrian A
Minster, J B
Bills, B G
et al.

Peer reviewed

Modeling Long-Period Noise in Kinematic GPS Applications

Adrian Borsa[1], Jean-Bernard Minster[1], Bruce G. Bills[1,2], Helen A. Fricker[1]

1.) Institute of Geophysics and Planetary Physics, Scripps Institution of Oceanography, University of California at San Diego, 9500 Gilman Drive, Mailstop 0225, La Jolla, CA 92093-0225
2.) Planetary Geodynamics Laboratory, NASA Goddard Space Flight Center, Greenbelt, MD 20771

Corresponding author: Adrian Borsa, aborsa@ucsd.edu, phone: 858-945-3806, fax: 858-534-2902

Abstract – We develop and test an algorithm for modeling and removing elevation error in kinematic GPS trajectories in the context of a kinematic GPS survey of the salar de Uyuni, Bolivia. Noise in the kinematic trajectory ranges over 15 cm and is highly autocorrelated, resulting in significant contamination of the topographic signal. We solve for a noise model using crossover differences at trajectory intersections as constraints in a least-squares inversion. Validation of the model using multiple realizations of synthetic noise shows an average decrease in root-mean-square-error (RMSE) by a factor of 4. Applying the model to data from the salar de Uyuni survey, we find that crossover differences drop by a factor of 8 (from an RMSE of 5.6 cm to 0.7 cm) and previously obscured topographic features are revealed in a plan view of the corrected trajectory. We believe that this algorithm can be successfully adapted to other survey methods that employ kinematic GPS for positioning.

Index terms – Global Positioning System (GPS), noise, kinematic GPS, inverse theory, salar de Uyuni

1. Introduction

Much of the contribution of the Global Positioning System (GPS) to the field of geodesy has come from millimeter-precision measurement of crustal deformation over periods of a day or longer (Dong and Bock 1989; 1993; Prescott et al. 2001). In these applications, batch processing of multiple-hour blocks of GPS data is typically used to establish a time series of positions for a fixed GPS antenna, with the temporal resolution of the method limited to the time span of the individual data blocks. Kinematic processing of GPS data is an alternative technique whereby a position is determined for the GPS antenna at every data epoch (Mader 1986). It is inherently less accurate than batch processing due to the smaller amount of information used to make each position estimate, but has the advantage of providing high-rate estimates of antenna position. Kinematic GPS is now the primary means of locating mobile geodetic survey instruments, including shipborne sensors for hydrographic sounding and sonar (e.g. Saka et al. 2004), airborne sensors for photogrammetry and laser altimetry (e.g. Krabill et al. 1995; Hofton et al. 2000; Gutierrez et al. 2001) and vehicle-mounted GPS antennas for direct surface height measurements (e.g. Phillips et al. 1998; Borsa 2005).

While the accuracy of elevation data obtained using kinematic GPS positioning surpasses that of generally available digital elevation models, the burgeoning application of topographic mapping to local surface change detection requires the ability to resolve vertical offsets on the order of decimeters (beach erosion, volcanic deformation) or even centimeters (ground subsidence, inland ice sheet changes) between consecutive surveys. In some instances, these requirements are clearly pushing the limits of kinematic GPS performance. Investigation of

kinematic GPS positioning of aircraft has found RMS elevation errors between 4 and 12 cm, along with biases that are often several times larger (Krabill and Martin 1987; Mader and Lucas 1989; Chen 1998). Kinematic processing of high-rate fixed antenna measurements reveals that GPS errors are highly correlated over periods of several minutes to hours (Georgiadou and Kleusberg 1988; Genrich and Bock 1992; Elósegui et al. 1995; Genrich and Bock 2006), which is mirrored by GPS noise characteristics at periods of one day to several years (Zhang et al. 1997; Mao et al. 1999; Williams et al. 2004). In the context of a mobile survey, correlated GPS noise will masquerade as long-wavelength topography and will contaminate any surface change signal. While local compensation for correlated GPS noise may be possible by aligning individual survey segments with one another or with independent ground reference, a systematic correction of the entire GPS trajectory is an attractive alternative.

This study discusses the mitigation of correlated GPS noise in the context of a kinematic GPS survey of salar de Uyuni, a massive salt flat in the Bolivian Altiplano whose surface elevation varies less than 1 meter over an area of almost 10000 km^2. The subtle topography that characterizes the salar is of interest from the standpoint of geodynamics and for the purpose of calibrating satellite-based radar and laser altimeters, yet is inadequately resolved by standard GPS post-processing because of the presence of GPS noise. To overcome this problem required a robust technique for modeling and removing long-period noise in the GPS solution. Although the flatness of the salar de Uyuni makes this a best-case scenario, we believe that our method can be easily extended to surveys of more complex terrain.

2. Data

2.1 Kinematic GPS Survey

We conducted a field campaign in September 2002 to map the topography of a 45×54 km region on the salar de Uyuni for the purpose of providing ground truth for NASA's Ice, Cloud and land Elevation Satellite (ICESat). The kinematic portion of the survey consisted of an array of eight identical survey grids (Figure 1), each of which was driven by a vehicle equipped with a dual-frequency Ashtech Z-12 GPS receiver, a roof-mounted Dorne-Margolin choke ring antenna and real-time GPS navigation. We also set up a network of fixed GPS stations on the salar (sites UY02~UY11) to provide ground truth and to serve as base stations for post-processing the kinematic trajectories. We operated the centrally-located UY04 continuously throughout the week-long campaign to provide a single local reference station for all GPS observations.

The survey grids consisted of parallel and perpendicular tracks spaced 2.25 km apart, whose intersections yielded over 100 crossovers per grid for estimating trajectory error (Figure 2). Each grid was driven in a single kinematic GPS session, with GPS receivers operating at a 3-second sampling rate and vehicle antenna heights measured pre- and post-session via an optical level. We post-processed the raw data for each survey grid with Track, the kinematic module of the GAMIT/GLOBK package (Chen 1998; Herring 2002), using the ionosphere-free LC observable double-differenced with respect to nearby fixed stations. We used a 10-degree elevation cutoff, precise IGS ephemerides and integer-only ambiguity values, which we found and set using Track's run-time diagnostics.

Post-processed trajectories for all survey grids exhibit elevation mismatches between crossing tracks, tracks that are consistently high or low for long distances, and elevation biases with respect to ground truth (Figure 3a). Since we correct for antenna height change due to fuel consumption and only include data for periods when inertial forces on the vehicle are low, antenna motion due to vehicle weight change and dynamic loading of the vehicle suspension should be minimal. We therefore assume that the source of the correlated survey errors is GPS measurement noise.

We estimated the magnitude of GPS noise from the analysis of elevation differences at trajectory crossover locations (Ridgway et al. 1997). In the absence of noise, all intersecting

points of the trajectory should have identical elevations and crossover differences of zero. Instead, most crossover differences are non-zero (Figure 4a). While the distribution of crossover differences on any given grid is nearly zero-mean, it is nominally Gaussian and has significant variance. The 115 crossover differences on Grid 2 of the survey, for example, have a mean of −0.3 cm and standard deviation (σ) of 5.5 cm.

Although noise on both tracks of a crossover contributes to a given crossover difference, if we assume that the noise on each crossing track is uncorrelated (which is generally the case), we can take the average along-track noise variance to be one-half the overall crossover difference variance. Under this assumption, along-track GPS noise on Grid 2 has $\sigma = 3.7$ cm and a range of about 15 cm at the 2σ (95.5%) level, which represents almost half of the 37 cm of total relief present in the GPS trajectory.

The plan view of Grid 2 elevations in Figure 3a clearly reveals the vertical offsets between intersecting tracks that are responsible for the non-zero crossover differences. Grid 2 also shows a pattern of highly-correlated elevations close in time (i.e., at nearby points along any single track) and less-correlated elevations distant in time (i.e., between crossing tracks), which indicates that most GPS noise in our survey is not random from epoch to epoch. This observation is consistent with the studies of GPS noise previously cited and implies that the temporal or spatial averaging techniques typically used to mitigate uncorrelated noise cannot be used here.

2.2 Fixed GPS Experiment

To isolate GPS noise from the topographic signal recorded by a moving antenna, we conducted a fixed-antenna experiment during the 2002 salar de Uyuni campaign. We collected contemporaneous data at 30-second sampling from three fixed sites on the salar (designated UYT1, UYT3 and UY10), which we post-processed relative to the continuously-operating central reference station UY04 (Figure 5). UYT1, which was placed 11 meters from UY04 to eliminate differential atmospheric effects, served as our experimental control. The antenna at UYT1 was mounted identically to the UY04 antenna, both of which were placed directly on the salar surface to minimize the impact of ground-reflection multipath (Elósegui et al. 1995). The antenna at UYT3 was mounted on the roof of a parked survey vehicle 30 km west of UY04 and served as a proxy for our high-multipath vehicle environment. Site UY10, 35 km to the northeast of UY04, was included primarily to estimate the tropospheric component of the GPS noise. Table 1 summarizes the mounting of all the experimental antennas and their baseline distances from UY04.

All sites operated Ashtech Z-12 receivers and Dorne-Margolin choke ring antennas identically aligned toward north. We post-processed the fixed site data in Track using the LC observable and the parameters specified for the kinematic data. Although Track does not accommodate meteorological observations, this mainly impacts the hydrostatic portion of tropospheric delay and is unlikely to have much effect over the constant vertical separations and the relatively short time span of this analysis. Track also does not yet have a provision for antenna phase-center mapping. Fortunately, the Ashtech antennae we used all have excellent phase-center stability and contribute no more than 0.3 mm error to the measured L1 and L2 phase over the range of observed elevations (Mader and MacKay 1997).

Figure 6 shows the post-processed elevation time series for an 8-hour period on 9/11/02 when the three experimental sites were operating simultaneously. Since we assume there is no relative surface motion between sites over this time period, we attribute all apparent antenna movement to GPS noise. The bottom time series in Figure 6 shows the low noise ($\sigma = 0.43$ cm) observed on the UY04−UYT1 control baseline, both relative to the other baselines and in absolute terms. Differential atmospheric effects between UY04 and UYT1 were eliminated by the short antenna baseline and multipath was effectively suppressed by ground mounting.

The increased noise in the UY10 time series ($\sigma = 0.92$ cm) shows the effect of increasing the baseline to 35 km. Analysis of the UY10 multitaper power spectrum (Figure 7)

demonstrates that this greater noise comes entirely from frequencies below 3×10^{-3} Hz (periods > 5 min), with the largest contribution from below 3×10^{-4} Hz (periods > 55 min). Since the antennae at UY10 and UYT1 are both ground-mounted at the same height, their multipath noise with respect to UY04 should be equivalent. With ionospheric error eliminated via the formation of the LC observable, unmodeled differential troposphere is the most likely source of the increased noise on the UY04UY10 baseline.

The UYT3 time series (Figure 6, top) has a standard deviation of 2.59 cm and a range of over 14 cm. This signal is so large and so strongly autocorrelated that it could easily be mistaken for real topography measured by a moving vehicle. It is also large enough to be the source of the observed noise on Grid 2 (Figure 3a). The UYT3 power spectrum (Figure 7) is particularly elevated at frequencies below 1×10^{-3} Hz (periods > 15 min), which is why the autocorrelation is so strong in the time domain. Since UY10 and UYT3 are approximately the same distance from UY04 and because the experiments are contemporaneous, we assume that the magnitude and autocorrelation of tropospheric errors on both baselines are roughly equivalent and that differential multipath is the likeliest source of the 10 dB of additional noise at UYT3.

Our results are broadly similar to the findings of Bock et al. (2000) and Genrich and Bock (2006), whose analysis overlaps ours in the frequency band between 10^{-2} and 10^{-4} Hz. The 2.53 cm standard deviation of vertical noise on the 31 km UY04–UYT3 baseline is smaller than that reported by Bock et al. (2000) for 30-second LC data using identical receivers and antennae on baselines of 50 m ($\sigma = 4.1$ cm, converted from interquartile range) to 37 km ($\sigma = 7.9$ cm). It is also smaller than that reported by Genrich and Bock (2006) for 1 Hz LC data on a 6 km baseline with identical equipment ($\sigma = 4.4$ cm). However, we believe much of this difference is due to the fact that the UY04 antenna in our pair was mounted directly on the surface and experienced negligible multipath.

In the spectral domain, our elevation data is represented by white noise at frequencies above 4×10^{-3} Hz and colored noise with a spectral index (Agnew 1992) of $-2 < \upsilon < -3$ at frequencies below this corner (Figure 7). The flattening of the spectra at the lowest frequencies may be an artifact of poor sampling; without a longer time series, we cannot draw any conclusions from the spectral densities in this band. Bock et al. (2000) find the same white+colored noise behavior, with similar corner frequencies between the two. They do not indicate a spectral slope for raw data, but it can be estimated from their figures to be around $\upsilon = -2$. Genrich and Bock (2006) also report white+colored noise, but find higher corner frequencies that may be due to lower aliasing from their higher sampling rates. Their estimates of spectral slope lie close to $\upsilon = -2$. Except for the exceptionally large spectral slope for UYT3 (which is in a vehicle rooftop environment unlike that of any other site studied) our spectra are consistent with those from these previous studies.

Although the parked vehicle at UYT3 only approximates the true kinematic GPS environment, we expect noise in our kinematic surveys to be statistically similar. Water vapor, which is the cause of most of the unmodeled tropospheric delay in the GPS signal, is spatially correlated over distances up to about 10 km (Macmillan 1995). Since this is about the spatial scale of the survey grids, vehicle motion should not introduce significant additional tropospheric error compared to the UYT3 results. Additional multipath noise on a moving car is also likely to be limited because 1.) the radar reflectivity of the salar surface is isotropic and varies little with location as the vehicle traverses the surface, and 2.) the reflectivity of the vehicle roof is nearly isotropic and is therefore minimally impacted by the changing orientation of a moving vehicle.

3. Theory

3.1 An Algorithm Based on the Minimization of Crossover Differences

To correct the kinematic survey trajectory for elevation error due to GPS noise, we introduce a noise modeling algorithm based on the minimization of trajectory crossover differences. The usefulness of crossover differences lies in the fact that the vector $h(x, y, t)$ of GPS elevations can be written as the sum of independent topographic and noise components:

$$h(x,y,t) = h(x(t),y(t))_{topo} + h(t)_{noise}. \tag{1}$$

In terms of (1), a crossover difference $d_{crossover}$ is formed by differencing the values of $h(x, y, t)$ at two separate times, but at the same location:

$$\begin{aligned} d_{crossover} &= \left[h\left(x(t_1),y(t_1),t_1\right) \right] - \left[h\left(x(t_2),y(t_2),t_2\right) \right] \\ &= \left[h\left(x(t_1),y(t_1)\right)_{topo} + h(t_1)_{noise} \right] - \left[h\left(x(t_2),y(t_2)\right)_{topo} + h(t_2)_{noise} \right] \\ &= h(t_1)_{noise} - h(t_2)_{noise} \end{aligned} \tag{2}$$

where t_1 and t_2 are the time values at which the GPS trajectory intersects the crossover location, and $h(x(t_1), y(t_1))$ and $h(x(t_2), y(t_2))$ cancel since they are at the same point on the surface. Since topography $h(x, y)$ is in the null space of the crossover differencing operation, the only way to generate non-zero crossover differences in this model is via noise on one or both of the crossing tracks.

Unfortunately, there is no information in the crossover difference about how the noise is distributed between the crossing tracks, which makes solving for a noise model using only crossover data an underdetermined problem with no unique solution. We do know from the UYT3 experiment, however, that GPS noise at our vehicle antenna has most of its spectral energy at long periods (i.e., it varies slowly in time). This means that a valid noise model $h(t)$ must be smooth in addition to adequately reproducing observed crossover differences. We could make the smoothness requirement rigorous by demanding that the noise model have the same power spectral density function as the UYT3 time series. In our algorithm, we opt to use the similar (yet simpler) target spectrum corresponding to the minimization of the first derivative of the noise model.

In the framework of a constrained optimization problem, finding a valid noise model can be summarized as

$$\text{minimize } \|\mathbf{D}q\|_2 \text{ subject to the constraint that } \|\mathbf{\Sigma}^{-1}(d - \mathbf{G}q)\| \le T \tag{3}$$

where the multipath model $q \in \mathrm{E}^N$ is a solution vector whose discrete values correspond to consecutive epochs of the multipath noise vector $h(t)$, $d \in \mathrm{E}^M$ is the vector of observed crossover differences, and $\mathbf{D}$, $\mathbf{G}$, $\mathbf{\Sigma}$, and T are defined below. The first part of (3) involves the smoothness requirement on the multipath noise model, which we enforce by minimizing $\|\mathbf{D}q\|_2$, the Euclidian norm (or 2-norm) of the first derivative of q. The derivative is numerically approximated by the first-difference matrix operator

$$\mathbf{D} = \mathrm{M}(N \times M) = \frac{1}{\Delta t}\begin{bmatrix} 0 & & & & & \mathrm{O} \\ -1 & 1 & & & & \\ & -1 & 1 & & & \\ & & & \ddots & \ddots & \\ \mathrm{O} & & & & -1 & 1 \end{bmatrix} \qquad (4)$$

with the time step Δt scaling the operator to treat large and small sampling intervals equally. The first-difference operator has a spectral index of $\upsilon = 2$, which is a line of slope 2 on a log-log power spectral density plot (Figure 8). The action of this operator in equation (3) is to preferentially select higher frequencies in q for minimization. As the minimization term is given greater weight in the inversion, the power spectrum of the calculated model q will increasingly resemble a line of slope -2, which is not quite as steep as the spectral slope observed for the UYT3 time series but is sufficient for imposing long-period correlation in the noise model.

In order to calculate the 2-norm numerically, we recast it in discrete terms. Using the definition of the 2-norm for continuous functions f

$$\|f\|_2 = \left(\int_{t_1}^{t_2} f(t)^2 \, dt \right)^{1/2} \qquad (5)$$

and the notion of numeric integration as a sum of discrete function values f_i with weights w_i corresponding to some integration scheme (we use Simpson's Rule)

$$\int_{t_1}^{t_2} f(t)^2 \, dt \cong \sum_i w_i f_i^2 \qquad (6)$$

we can write the 2-norm in matrix form as (Parker 1994, p.164)

$$\|\mathbf{D}q\|_2 = (q \cdot \mathbf{DWD}q)^{1/2} \qquad (7)$$

where $\mathbf{W}$ $diag(w)$.

The second part of (3) is the misfit criterion $\|\mathbf{\Sigma}^{-1}(d - \mathbf{G}q)\| \leq T$, which requires that the model predictions $\mathbf{G}q$ match the crossover differences d to within a tolerance limit T. We write this using the inner (dot) product notation $\|\cdot\|$. $\mathbf{G} \in \mathrm{M}(N \times M)$ is a design matrix that selects positions along the time-valued model q corresponding to the locations of the crossovers whose differences appear in d. $\mathbf{G}q$ has the form

$$\mathbf{G}q \in \mathrm{E}^M = \begin{bmatrix} 0 & 1 & 0 & \dots & 0 & -1 & 0 & \dots & 0 & 0 \\ 0 & 0 & 1 & 0 & 0 & & \dots & 0 & 0 & -1 & 0 \\ & & & & (etc) & & & & & \end{bmatrix}\begin{bmatrix} q_1 \\ q_2 \\ q_3 \\ q_4 \\ \vdots \\ q_N \end{bmatrix} \qquad (8)$$

6

with the 1, −1 pairs acting as operators that subtract the chronologically later model values from the earlier ones, which is exactly how the crossover differences in d are calculated. $\Sigma \in M(M \times M)$ is the diagonal matrix $diag(\sigma_{crossover})$ used to normalize each constraint by the standard error of its crossover difference, thereby allowing the model misfit measure to vary according to the quality of each datum.

The tolerance T explicitly addresses the question of how far d should deviate from $\mathbf{G}q$. Since we do not want the model to fit the measurement noise in d, the term $\left\| \Sigma^{-1}(d - \mathbf{G}q) \right\|$ should be strictly positive. If we write d as the sum of a true crossover difference d_{true} fit exactly by $\mathbf{G}q$ and a random error term e (i.e., d $d_{true} + e$), then the tolerance limit we should choose is the expected distance of e from the origin:

$$T = E\left[\left\| \Sigma^{-1}(d_{true} + e - \mathbf{G}q) \right\|\right] = E\left[\left\| \Sigma^{-1}e \right\|\right]. \tag{9}$$

Taking $\Sigma^{-1}e$ to be a Gaussian random vector with unit standard deviation (since e is normalized by the crossover variances in Σ), and noting that N is the number of crossover differences being fit, we can use the result (Parker, p.124)

$$T = N^{1/2}\left[1 - \frac{1}{4N} + \frac{1}{32N^2} + O\left(N^{-3}\right)\right]. \tag{10}$$

With these descriptions, solving the minimization problem stated in (3) involves finding the stationary values of

$$U(q,v) = \left(\left\| \mathbf{D}q \right\|_2\right)^2 - v\left(T^2 - \left\| \Sigma^{-1}\left(d - \mathbf{G}q\right)\right\|^2\right) \tag{11}$$

which is a slightly-modified form of the standard equation used in the method of Lagrange multipliers. Here, the Lagrange multiplier v is a positive-valued parameter that determines the trade-off between model smoothness (the first term) and model misfit (the second term). Since the stationary values of U occur when its gradient vanishes, we seek v and q such that

$$\nabla U(q,v) = \nabla\left(q \cdot \mathbf{D}^T\mathbf{W}\mathbf{D}q\right) - v\nabla\left(T^2 - \left\| \Sigma^{-1}\left(d - \mathbf{G}q\right)\right\|^2\right) = 0 . \tag{12}$$

To solve this problem, we treat the Lagrange multiplier v as a constant and differentiate U with respect to q (Parker, p.165)

$$\left(\mathbf{G}^T\Sigma^{-2}\mathbf{G} + v^{-1}\mathbf{D}^{-1}\mathbf{W}\mathbf{D}\right)q = \mathbf{G}^T\Sigma^{-2}d . \tag{13}$$

Satisfying the tolerance criterion for the model misfit requires fixing v at a range of values, each time solving (13) for q and calculating the misfit $\left\| \Sigma^{-1}(d - \mathbf{G}q)\right\|$. Once we know the approximate value of v that generates a misfit close to T, we use a modified form of Newton's method to converge on the best-fitting q and v.

3.2 Crossover Difference Calculation

The algorithm we use to determine crossover differences is particularly suited to the flatness of the topography on the salar de Uyuni. Our method is an adaptation of the procedure

developed by Rowlands et al. (1999) for the Mars Orbiting Laser Altimeter (MOLA) mission. We fit straight lines to the coordinates of individual GPS epochs on pairs of crossing tracks and analytically solve for all the geographic crossover locations within a single GPS trajectory (Figure 9). For each crossover, we then take all epochs within 500 m of the crossover location and linearly interpolate elevations on each track to obtain the crossover elevations z_1 and z_2. The crossover difference $d_{crossover}$ is defined as the difference $z_1 - z_2$. The details of the calculation are shown in Appendix A, along with a derivation of the crossover standard deviations that appear on the diagonal of Σ in (3). Although more complex topography would require higher-order polynomials to accurately fit the trajectory and a different calculation for the crossover standard deviation, the conceptual framework for the difference calculation would remain unchanged.

3.3 Using Tiepoints to Further Constrain the Model

The algorithm described above can be improved by the explicit inclusion of tiepoints between the kinematic trajectory and fixed GPS sites. Differences between trajectory elevations and the (known) fixed site elevations give the exact value of the noise model at certain points in time. This can significantly strengthen the constraints in the noise model inversion, since crossover differences alone cannot distinguish noise on individual survey tracks. We implement tiepoint differences in the algorithm by extending the crossover vector d to include the tiepoint differences values and expanding the design matrix $\mathbf{G}$ in (8) to include an extra row for each tiepoint. These rows have a solitary 1 in the position corresponding to the location along the noise model where the tiepoint comparison takes place. We similarly expand Σ to include the standard error of each tiepoint comparison.

4. Results

4.1 Testing the Algorithm

We validated the noise modeling algorithm using synthetic data on a standard survey grid. For the tests described below, we replaced GPS elevation measurements from Grid 2 with synthetically-generated topography and noise, calculated crossover and tiepoint differences, and inverted for a noise model. Using the trajectory from an actual survey grid allows us to make very specific predictions about how well the algorithm should work in the context of the salar de Uyuni survey.

Our synthetic topography is drawn from three sample terrains: 1) a flat plane (which approximates the actual salar topography); 2) a broad cylindrical valley; and 3) a random surface with a "red" two-dimensional power spectrum. For a given synthetic surface we calculate the topographic elevations that correspond to our actual vehicle trajectory on Grid 2. This is our "observed" topographic time series. To this time series we add synthetic noise whose power amplitude spectrum is equivalent to that of the UYT3 time series.

For the first series of tests we assumed flat topography (i.e. $h(t) = 0$) and replaced the Grid 2 survey elevations with 12 different realizations of synthetic noise, which we generated using a generalized form of the Fourier transform technique described in Pilgrim and Kaplna (1998). We calculated crossover and tiepoint differences due to the noise signal exactly as if we were using survey data and solved for noise models based on 1.) crossovers alone and 2.) both crossovers and tiepoints. Figure 10a shows the results of Test 9, with the noise model calculated using crossovers only. In the top panel we plot the synthetic data as individual points, the calculated noise model as a solid line and the location of crossover constraints as vertical ticks on the zero line. Crossovers are grouped in sets separated by short gaps, with each grouping corresponding to crossovers on a single track across the survey grid. Although the noise model is not constrained in the gaps between crossover sets, this does not appear to significantly affect

the model. The model residual in the bottom panel of Figure 10a shows that the noise model generally follows the synthetic data, but lies uniformly above it for the entire time span.

The primary effect of including tiepoints is to remove the bias between model and data. Figure 10b shows that the constraints provided by the tiepoint differences indicated as red triangles force the model to shift downward by about 0.75 cm. We note that including tiepoints did not improve the model at the beginning of the time series, where crossovers appear to impose insufficient constraint on the inversion. An additional tiepoint here might have helped to locally adjust the model toward its correct value.

The power spectra for Test 9 (Figure 11) shows that variance reduction in the model residual is the result of a significant attenuation of power at periods of 15 minutes and longer. Although this is the bulk of the noise, the fact that we cannot model noise at shorter periods has implications that we address in the discussion below. We also note that there is little difference between the residual spectra for models with and without tiepoints, confirming that the main effect of tiepoints is the vertical (i.e. DC) shift of the model.

The results for all synthetic time series are similar to that of Test 9 (Table 2). In all cases, the algorithm adequately models the long-wavelength noise error, with misfits remaining at shorter wavelengths. Using crossovers alone, we reduce the average RMSE more than threefold, from 3.47 cm to 1.02 cm. Incorporating tiepoints further lowers the average RMSE to 0.94 cm, although 5 of 12 individual tests actually saw a rise in this measure. Overall, these results suggest that the algorithm is quite robust. Despite significant differences between the shapes of the different synthetic noise time series, the worst RMSE (with tiepoints) is only 1.25 cm.

To confirm our assumption in (2) that topography does not appear in the crossover datum and therefore should not alter our findings, we duplicated our tests using synthetic topography from both the cylindrical and random red-spectrum surfaces. We find that cylindrical topography with amplitude less than 100 m has almost no impact on the model solution. Random topography with amplitude greater than 1 meter begins to introduce error in the model due to the fact that our crossover difference calculation fits topography with short line segments that inadequately represent the surface. Although the linear approximation is adequate for crossovers on the salar, it is increasingly inaccurate as local curvature increases and may require modification for surveys of more commonly encountered geological surfaces.

4.2 GPS Noise Reduction in the salar de Uyuni Survey

We achieved excellent results applying the noise modeling algorithm to actual GPS data from Grid 2 of our salar de Uyuni survey (Figure 3b). Comparison with uncorrected data (Figure 3a) shows that crossing tracks now agree at crossover locations, survey elevations are consistent with fixed sites, and subtle topographic features can be identified across multiple tracks. Although crossover differences in Grid 2 are reduced by a factor of 8 (from σ = 5.5 cm to σ = 0.7 cm), it is the presence of a spatially coherent topographic signal that is the most important validation of the noise modeling algorithm. There are an infinite number of possible models that could minimize crossover differences without reproducing the true noise signal, yet it is extremely unlikely that any of these would cause the corrected elevations to be spatially correlated across multiple survey tracks.

Another perspective on the Grid 2 improvement is given by comparing the time series of GPS elevations in Figure 4a with the corrected version in Figure 4b. Not only have the three highlighted crossover differences been reduced to nearly zero, but the trajectory also lies very close to the planar surface indicated by the solid line, which is consistent with the lack of visible topographic relief on the salar. We take the observations in Figures 3 and 4 as strong evidence that the noise modeling algorithm has succeeded in recovering the GPS noise contaminating the kinematic survey results.

Although we assume the vehicle rooftop to be an isotropic radar reflector in order to model GPS (multipath) noise as a slowly-varying function of time, we did an additional test to confirm that abrupt changes in the GPS satellite constellation at vehicle turns were not impacting the noise solution. We decoupled the noise model between tracks of the survey grid by introducing a

row of zeros in the first-difference matrix **D** whenever the vehicle made a 90-degree turn. This preserved model smoothness on each track, while allowing jumps in the noise model between tracks. Running this modified modeling algorithm on the actual survey data for Grid 2 resulted in negligible differences in the noise model.

5. Discussion

5.1 Crossover Distribution

Since we had originally planned to use crossovers for survey error estimation only, we did not design our survey grids with any consideration given to the optimal crossover distribution for noise modeling. We now address that question by considering GPS noise with power distributed in some way across the frequency spectrum. Nyquist's Theorem tells us that we can only model the portion of this signal at frequencies lower than $1/(2\Delta T)$, where ΔT is the sampling interval of our noise measurements. Any part of the signal at frequencies higher than this will be aliased into lower frequencies in the model.

For the salar survey, the spectrum of the stationary UYT3 vehicle antenna (Figure 7) suggests that over 95% of noise power should come from frequencies below 0.001 Hz. Based on the Nyquist criterion, a ΔT of 8 minutes should therefore be adequate to model noise in the GPS trajectory. The problem with this assumption is that we do not have direct measurements of the noise signal except at tiepoints. Crossover differences contain only half the information of a direct noise measurement and thus act as a series of looser constraints on the noise.

The modeling tests in section IV give us some insight on the relationship between crossover spacing and model resolution, however. At a driving speed of 120 km/hr and nominal crossover spacing of 2.25 km, we average about one crossover per minute on our survey grids (i.e., ΔT 1 minute, where we take ΔT to refer to the temporal crossover spacing). If the Nyquist criterion were valid, we would be able to model noise down to a period of 2 minutes. The fact that we only achieve noticeable noise reduction at periods of 15 minutes and longer is evidence that crossovers are a much less rigorous constraint on the noise model than are actual noise measurements. We cannot say without explicit modeling what crossover spacing should be for a given application, but suggest that for kinematic GPS survey like ours, spacing should be as small as is feasible.

In addition to providing a large number of crossovers, our survey grid design ensures that the track pairs in each crossover are (on average) widely spaced in time. This temporal spacing guarantees that the noise on crossing tracks is uncorrelated, which avoids having (correlated) noise canceling in crossover differences. This is important because the information provided by a crossover difference concerns the uncorrelated portion of the noise and is lost if noise is not independent on crossing tracks.

5.2 Tiepoint Distribution

Tiepoints are a critical element of the algorithm. The inherent ambiguity in the crossover difference datum means that the algorithm relies on the inability of most models in the solution space to both satisfy the smoothness criterion and fit the crossover data. Even for a survey with a dense network of crossovers, however, we occasionally find that the algorithm favors models which consistently under- or over-estimate the actual noise for considerable periods (possibly due to correlation between noise on crossing tracks). Tiepoints correct this problem by pinning the noise model to its correct value at points along the trajectory. We have not determined the optimal number or spacing of tiepoints, but at a minimum there should be one area of ground truth during a survey that is periodically revisited. We also point out that for surveys with temporal gaps in crossover coverage, it is possible to add tiepoints later by surveying locations along the original trajectory where model constraints are needed.

10

5.3 Model Smoothing

While the choice of ΔT in the crossover/tiepoint distribution helps to determine which frequencies are excluded from the noise model, the smoothing criterion determines how power in the model is distributed between the frequencies that are present. In the case of the first-difference smoothing we use, the model will tend toward a power-law function with $\upsilon = -2$. If the actual noise has a very different spectral index (or if its spectrum deviates significantly from a power-law model) we can expect error in the noise model. In similar applications of constrained minimization, however, we have observed that the choice of first or second derivative minimization yields very similar models even though the implied spectral index for second-derivative models is twice as large ($\upsilon = -4$).

6. Conclusions

The algorithm we have presented here is an attempt to address important noise-related limitations of GPS for geodetic-quality kinematic positioning. We believe that this approach can be generalized to other applications that employ kinematic GPS for positioning. In airborne laser swath mapping (ALSM), for example, the additional complication of interposing a laser subsystem between the GPS and the ground should not change the noise modeling approach substantially, since proper calibration of the laser instrument allows GPS elevation error to be handled independently of other system errors. Any location where survey swaths cross or overlap is a candidate crossover location, which means that most airborne surveys are already configured to take advantage of the noise modeling algorithm. Our own future work will test the algorithm on ALSM data from a survey of the Bonneville Salt Flats, where the aircraft trajectory contains numerous crossovers and where we have excellent ground truth over much of the survey area.

Acknowledgements

Appendix A. Crossover Differences and Statistics

The linear regression used to find the heights along each crossing track in a crossover (c.f. Figure 9) fits the linear model $z = a + bx$ to pairs of UTM eastings (or northings) x_i and elevations z_i by minimizing the chi-square

$$\chi^2(a,b) = \sum_{i=1}^{N} \frac{(z_i - a - bx_i)}{\sigma_i^2}. \tag{A1}$$

This is done separately for both crossing tracks, obtaining two sets of parameters a and b. For each track, the crossover height z_c is estimated by evaluating $a + bx$ at the x coordinates of the crossover. The crossover difference is defined to be the difference between the two crossover heights $(d_{crossover} \equiv z_{c1} - z_{c2})$.

The denominator of Equation (A1) explicitly includes the variance of each elevation in the linear regression. This is a difficult quantity to estimate, since the noise sources contributing to variability in z_i are quite varied. However, we are interested only in uncorrelated error, since correlated error is addressed by the GPS noise modeling algorithm. One estimate of average uncorrelated error on a GPS trajectory is the variance of elevation differences between consecutive epochs. This estimate of uncorrelated noise variance can be written

$$\hat{\sigma}^2 = Var\big(h(t) - h(t + \Delta t)\big) = E\Big[\big(h(t) - h(t + \Delta t)\big)^2\Big] - E\Big[\big(h(t) - h(t + \Delta t)\big)\Big]^2 \tag{A2}$$

where $E[\,]$ is the expectation operator, $h(t)$ is the survey elevation at time t, and $h(t + \Delta t)$ is the elevation one epoch later. Since the expectation of a finite sample of data is just the sample mean, the right hand side of (A2) can be rewritten in terms of the T surveyed elevations h_t and their counterparts h_{t-1} (lagged by one epoch)

$$\hat{\sigma}^2 = \frac{1}{T}\sum_{t=1}^{T}(h_t - h_{t-1})^2 - \frac{1}{T^2}\left(\sum_{t=1}^{T}h_t - \sum_{t=1}^{T}h_{t-1}\right)^2. \tag{A3}$$

Equation (A3) gives the epoch-to-epoch variance for the GPS trajectory, from which we obtain an average standard deviation estimate to use for all σ_i in (A1).

An expression for the uncertainty in the crossover difference estimate (which combines the error from each of the intersecting trajectories) can be derived from the uncertainty in the parameters of the chi-square metric. Numerical Recipes (Press et al. 1992) gives a thorough treatment of the linear regression problem and we use the relevant results here. Subtracting the mean value of x from all the x_i's in the linear regression and assuming a constant variance equal to the estimate from (A3) gives the variance and covariance of parameters a and b as:

$$\sigma_a^2 = \hat{\sigma}^2 / N \tag{A4}$$

$$\sigma_b^2 = \hat{\sigma}^2 \bigg/ \left(N\sum_{i=1}^{N}x_i^2\right) \tag{A5}$$

$$Cov(a,b) = 0 \tag{A6}$$

The zero covariance between parameters a and b allows us to write the variance of each height in the crossover difference as

$$Var(z_c) = Var(a + bx) = Var(a) + x^2 Var(b) = \sigma_a^2 + x^2 \sigma_b^2 \tag{A7}$$

where x is the position along the line corresponding to the crossover location. The uncertainty in the crossover difference is

$$\sigma_{crossover} = \sqrt{Var(z_{c1} - z_{c2})} = \sqrt{Var(z_{c1}) + Var(z_{c2})} \tag{A8}$$

where we use (A7) to evaluate each term on the right hand side separately. The $\sigma_{crossover}$ values from (A8) become the diagonal entries of Σ in Equation (3).

Tables and Figures

Table 1. Results from fixed antenna experiments.

Antenna Pair	Antenna Mounting Convention	Baseline Distance	Standard Deviation of Time Series
UY04–UYT1	Ground-Ground	11 m	0.43 cm
UY04–UY10	Ground-Ground	35 km	0.92 cm
UY04–UYT3	Ground-Car	31 km	2.59 cm

Table 2. Results from testing the noise-modeling algorithm.

Test #	Synthetic noise RMSE (cm)	Model w/o Tiepoints Residual Mean (cm)	Model w/o Tiepoints Residual RMSE (cm)	Model with Tiepoints Residual Mean (cm)	Model with Tiepoints Residual RMSE (cm)
1	3.38	-0.38	0.98	0.12	0.85
2	2.56	-0.43	0.94	0.05	0.72
3	3.19	-0.28	0.85	0.41	0.89
4	3.89	-0.28	0.81	-0.57	0.94
5	4.12	0.20	0.94	0.13	0.85
6	3.60	-0.01	0.98	0.41	1.01
7	3.23	-0.53	0.98	0.31	0.89
8	3.66	-1.06	1.33	0.06	0.81
9	3.04	-0.84	1.11	-0.09	0.72
10	4.48	-0.50	1.06	-0.79	1.23
11	4.10	-0.27	0.96	0.87	1.25
12	2.34	-0.45	1.25	-0.09	1.15
Avg.	3.47	-0.40	1.02	0.07	0.94
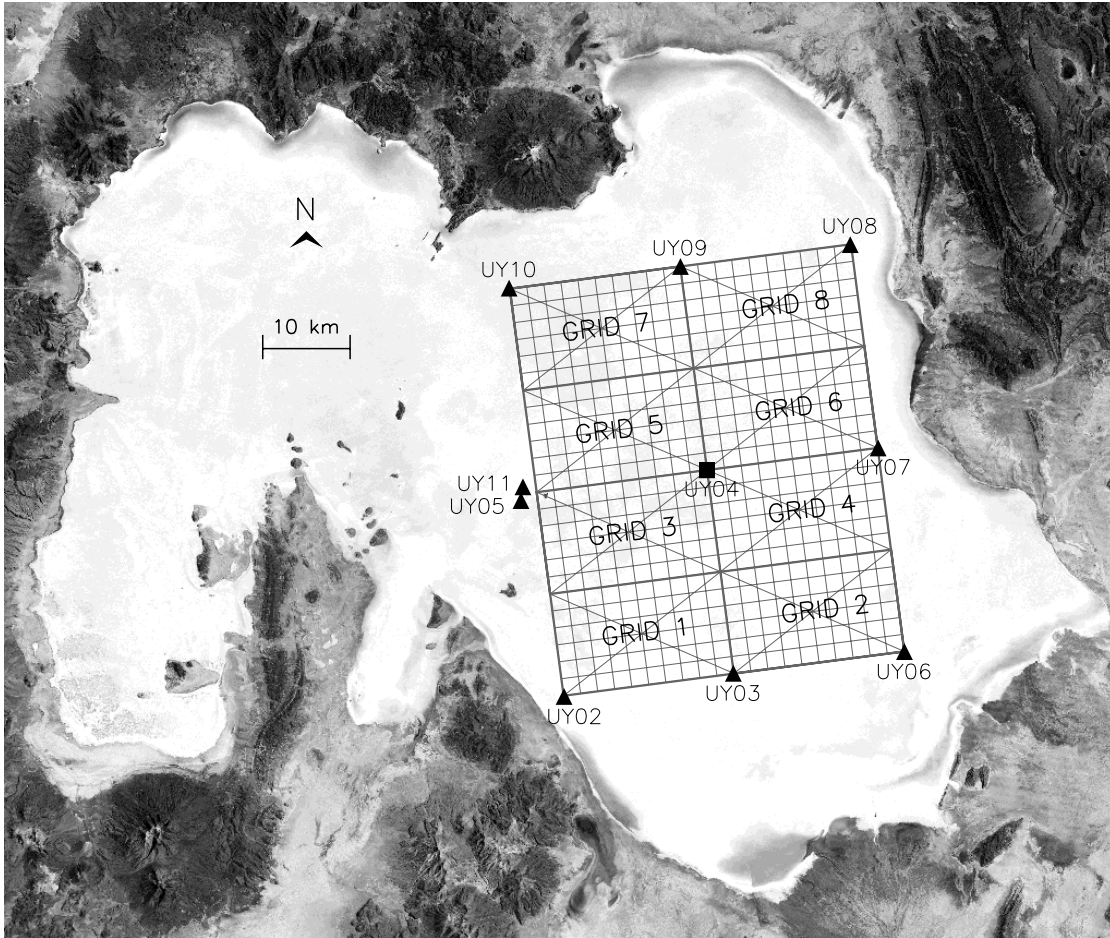
Figure 1. Landsat image of the salar de Uyuni, overlaid with the major components of the GPS survey. Fixed GPS sites UY02~UY11 are shown as triangles, the reference site UY04 is shown as a square, and survey grids 1~8 are indicated by their survey tracks. Topographic relief is about 80 cm across the entire survey area.
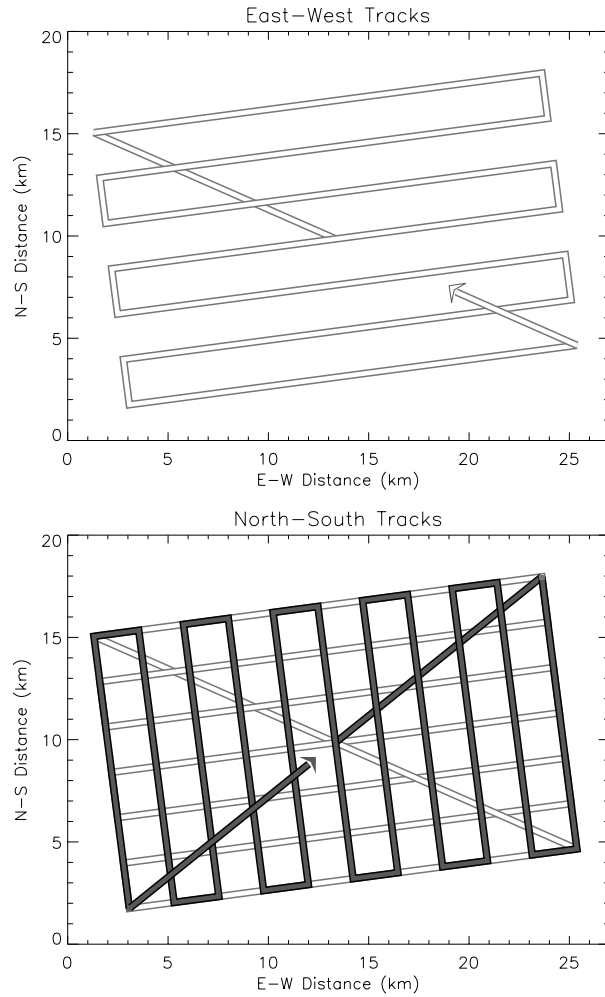
Figure 2. Survey grid driving pattern. (Top) The vehicle starts at the grid center, goes directly to the northwest corner, and drives back and forth along the east-west legs. (Bottom) It then repeats this pattern along the north-south legs. Across-track spacing is 2.25 km.
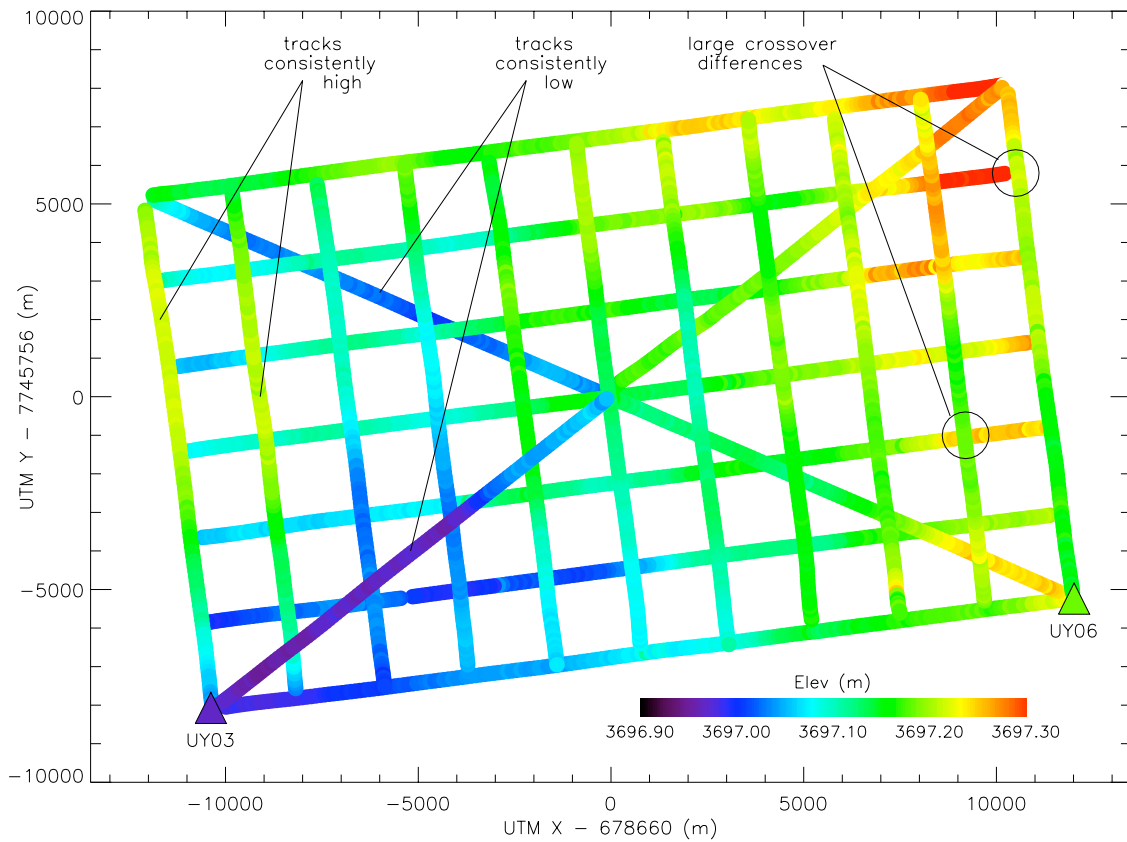
Figure 3a. Post-processed survey elevations from Grid 2. GPS noise manifests itself in large crossover differences ($\sigma = 5.5$ cm) and survey tracks that are high or low compared to adjacent tracks. Other than the broad slope to the NE, it is difficult to identify topographic features in the data. The elevations of fixed sites UY02 and UY06 (given by the color of the filled triangles) are consistent with only some of the tracks that pass nearby. Overall grid dimensions are 22.5×13.5 km.
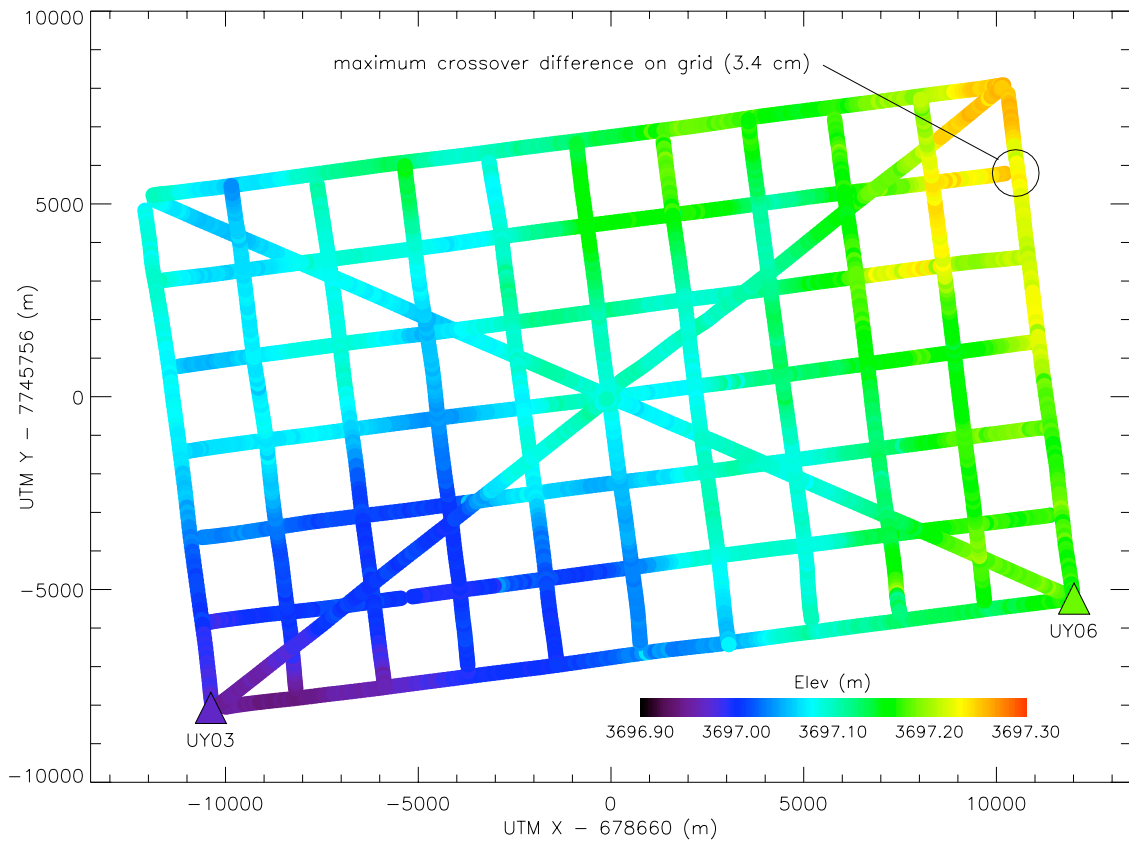
Figure 3b. Survey elevations on Grid 2 after correction for GPS noise model calculated in this paper. Crossover differences have been nearly eliminated ($\sigma = 0.6$ cm) and survey tracks near UY02 and UY06 agree with the fixed site elevations. Subtle, spatially-coherent topographic features can be identified across multiple survey tracks.
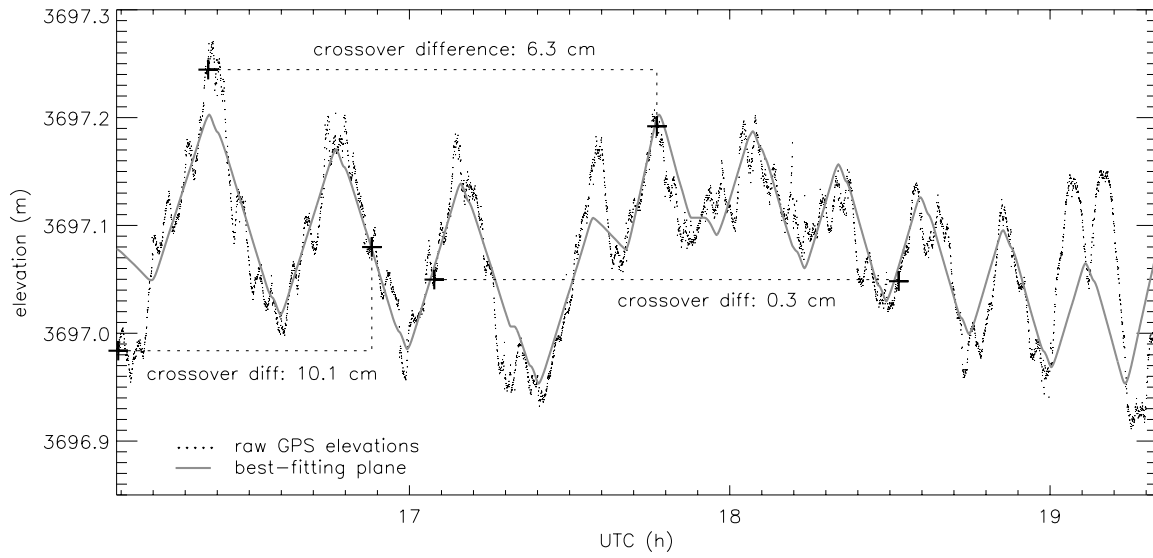
Figure 4a. Time series of raw survey elevations from Grid 2, with three crossover pairs shown in blue. The offset between crossovers in each pair gives the crossover difference and indicates GPS noise on one or both survey tracks. The solid line indicates the best fitting plane to the elevation data. Actual topography should not deviate far from this line, given the flatness of the salar.
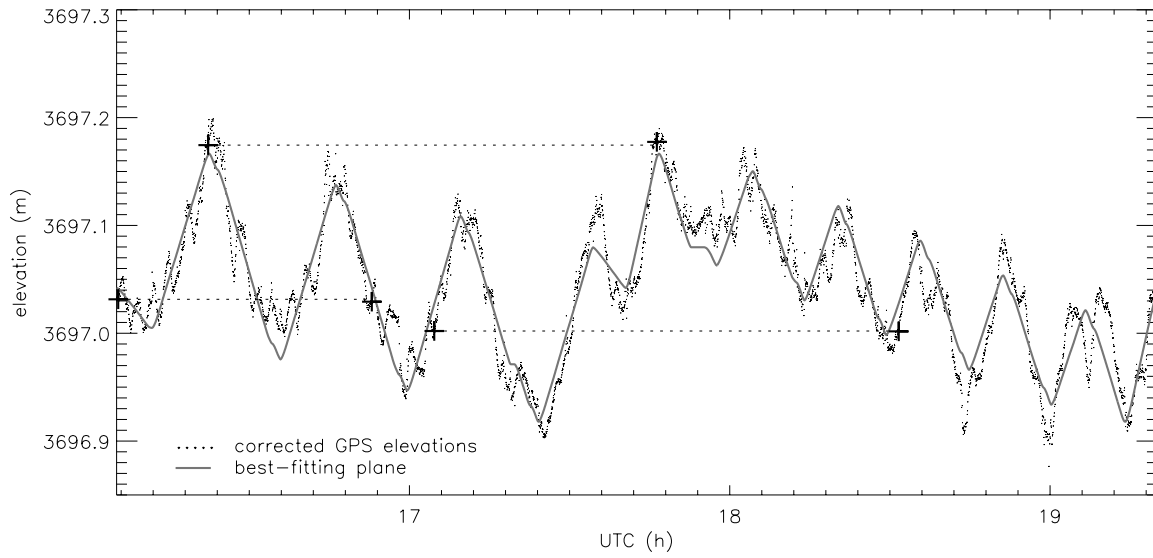
Figure 4b. Same as for Figure 4a, but for noise-corrected elevations. Applying the noise model gives an elevation time series whose crossover differences are all nearly zero (all the crossovers now lie at the same elevation) and which much more closely approximates the topography of a simple plane.
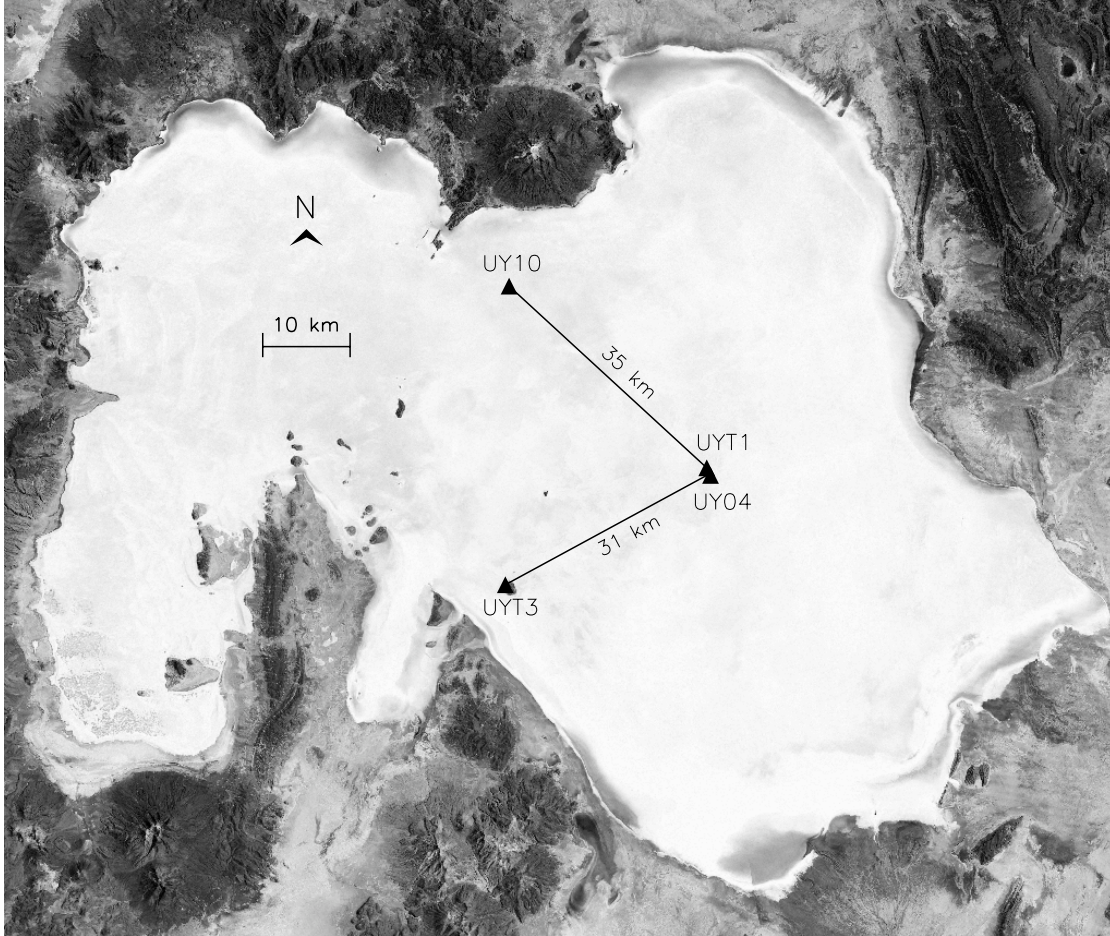
Figure 5. Locations of, and baseline distances between, the GPS noise experiment sites on the salar de Uyuni. UYT1 incorporates a ground-mounted antenna situated 11 meters from the UY04 reference site. UY10 is one of the ground-mounted fixed sites used for the kinematic survey, and UYT3 is a GPS installation on one of our survey vehicles. All three sites use Dorne-Margolin choke-ring antennae and Ashtech Z-12 receivers.
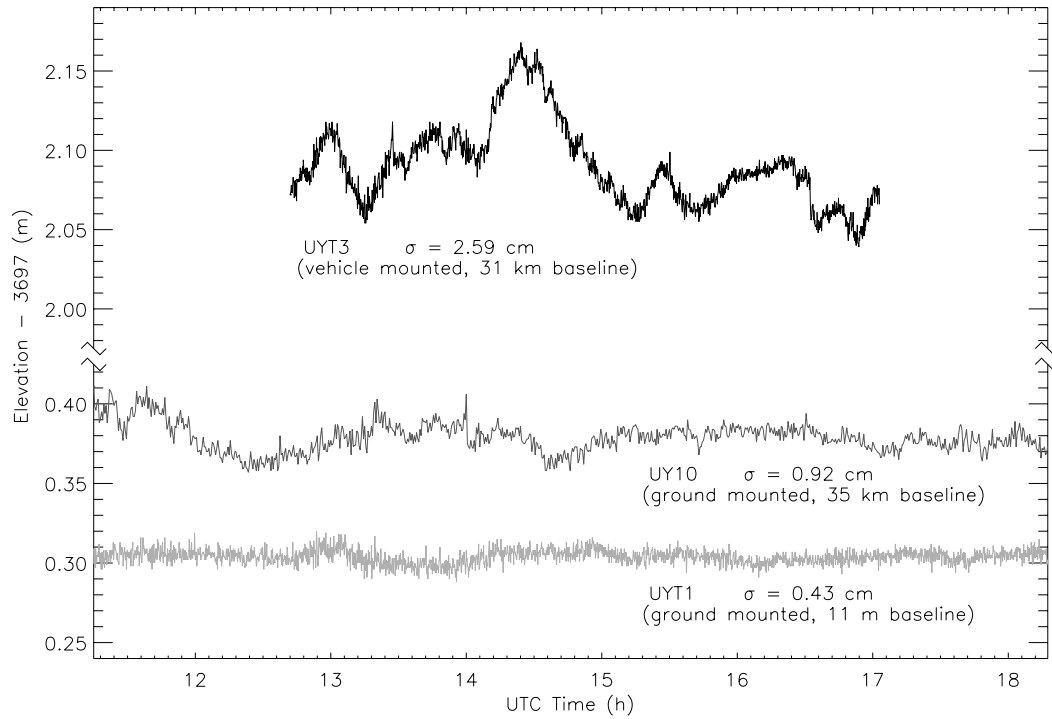
Figure 6. Elevation time series (30-second sampling) for the three sites shown in Figure 5, processed with respect to reference site UY04. Since all antennae are fixed, apparent antenna motion is due to GPS noise alone. The time series for UYT1 and UY10 show how GPS noise for ground-mounted antennae increases with baseline distance (11 m and 31 km, respectively), while remaining small in absolute terms. The UYT3 time series approximates noise at the kinematic antennae and shows that this noise is much larger in magnitude and is strongly autocorrelated.
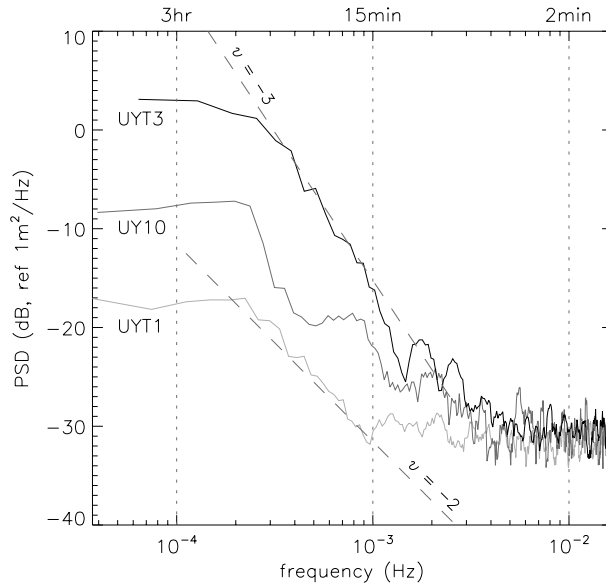
Figure 7. Power spectral density (PSD) functions for all three time series in Figure 6, estimated using multitaper spectral averaging, with the multitapers normalized to conserve power. Tropospheric delay results in about 10dB higher noise at UY10 compared to UYT1 for periods longer than 15 minutes. The 10dB additional noise at UYT3 is due to strong multipath from the vehicle rooftop. Dashed lines indicate the spectral slopes corresponding to PSD functions with spectral indices $v = -2$ and $v = -3$.
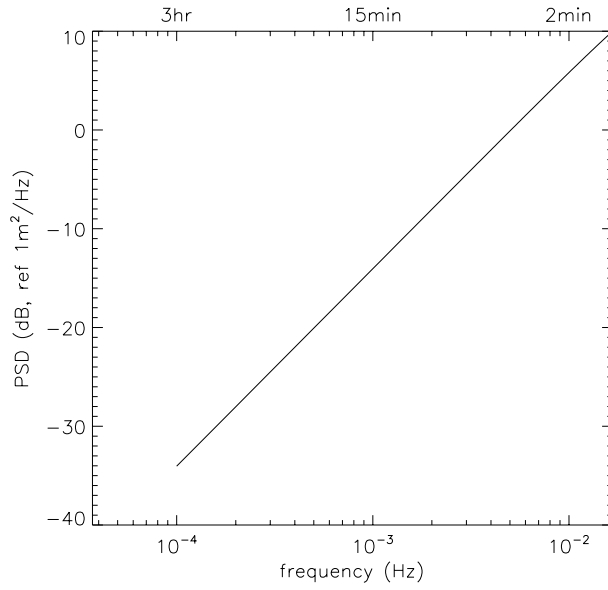
Figure 8. Power spectral density function of the first-difference operator in Equation (4), normalized to unit variance. The operator has a spectral index of 2, which means that the inversion will preferentially return noise models with a spectral index approaching -2 (i.e. random walk noise) as the first-difference minimization term is given increasing weight.
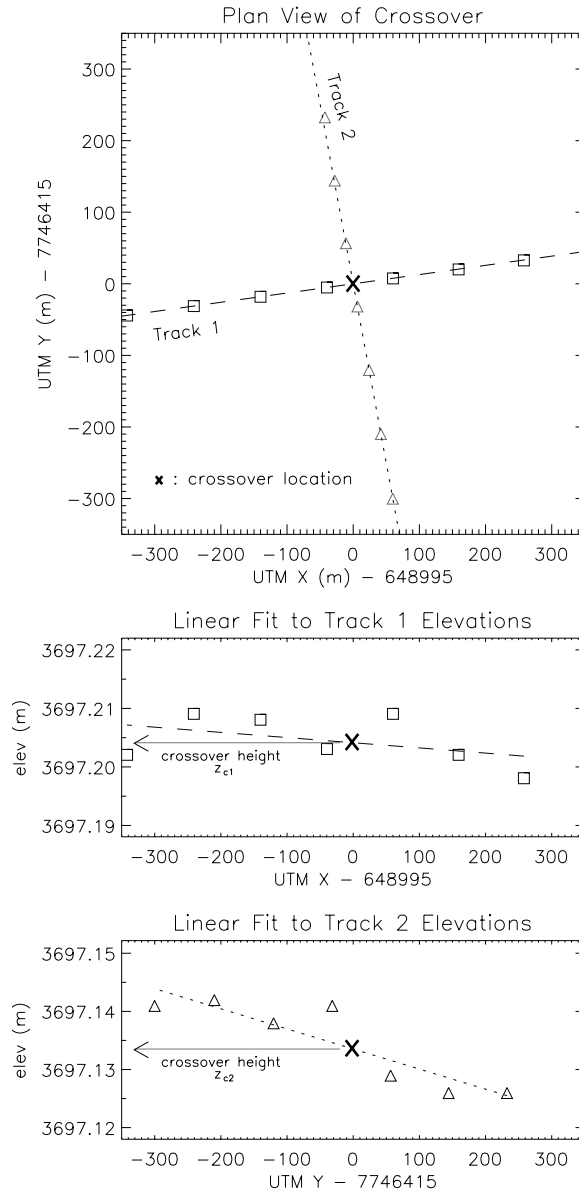
Figure 9. Crossover difference determination for a crossover on Grid 2. (Top) Lines are fit to the horizontal coordinates of points on crossing tracks of the GPS trajectory. Their intersection becomes the crossover location. (Middle) A linear fit to elevations from Track 1 is performed, with the elevation at the crossover location taken as crossover height z_{c1}. (Bottom) The same process is repeated for Track 2 to get crossover height z_{c2}. The difference $z_{c1} - z_{c1}$ gives the crossover difference at this location.
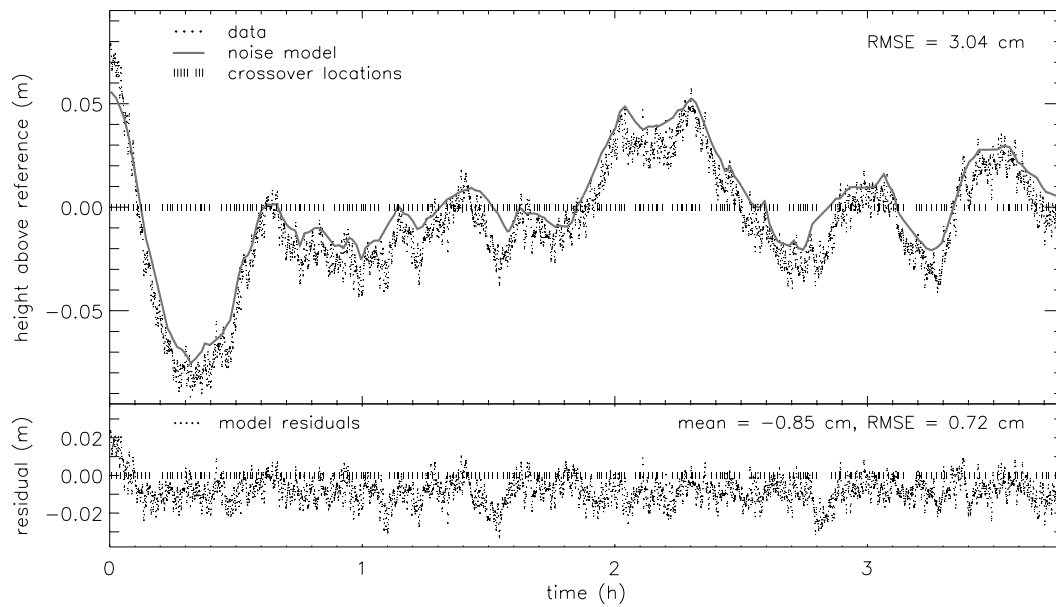
Figure 10a. Results from testing the noise algorithm using synthetic data, assuming a constant-valued topographic surface. Shown are results from Test 9, evaluated without tiepoints. Top panel shows synthetic noise data (individual points), the noise model (solid line) and the locations of crossovers used in the algorithm (vertical ticks on the zero line). Bottom panel shows the model residuals on the same scale. Although the data RMSE is reduced by a factor of 4 by removing modeled noise, the non-zero mean of the residual indicates model bias.
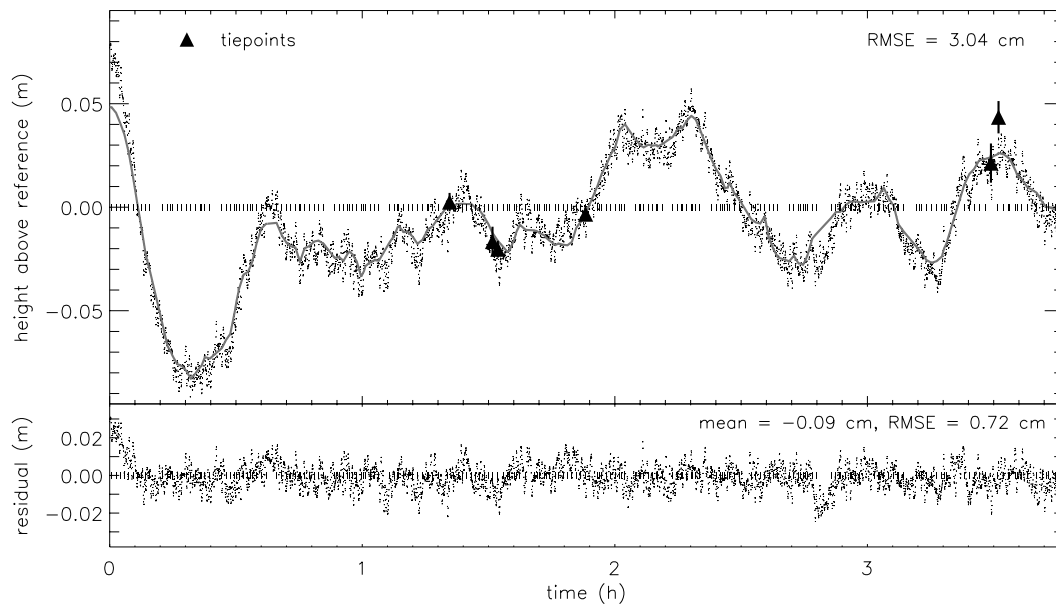
Figure 10b. Same as Figure 10a, but with tiepoints included in the model calculation. Filled triangles indicate tiepoint locations along the GPS trajectory and the corresponding tiepoint differences, with error bars showing the 1σ error limits of the tiepoint difference calculation. The model passes through or near most tiepoints, reducing the model bias to nearly zero. RMSE remains unchanged.
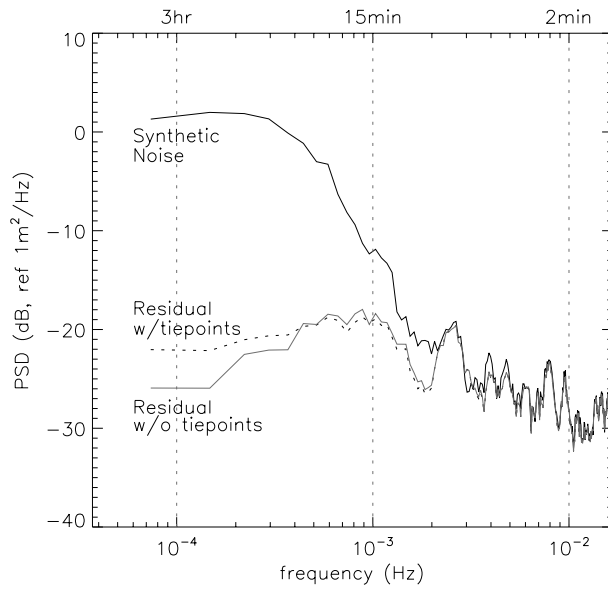
Figure 11. Power spectral density functions for the test data shown in Figure 10 (by design, the synthetic noise spectrum is identical to that of UYT3). The spectra of the model residuals show that removing the noise model dramatically attenuates power at periods of >15 minutes, which is where GPS noise is greatest (Figure 7).

References

Agnew, D. C. (1992). "The time-domain behavior of power-law noises." <u>Geophysical Research Letters</u> **19**(4): 333-336.

Bock, Y., D. C. Agnew, P. Fang, J. F. Gengrich, B. H. Hager, T. A. Herring, K. W. Hudnut, R. W. King, S. C. Larsen, J.-B. Minster, K. Stark, S. Wdowinski and F. K. Wyatt (1993). "Detection of crustal deformation from the Landers earthquake sequence using continuous geodetic measurements." <u>Nature</u> **361**(6410): 337-340.

Bock, Y., R. M. Nikolaidis, P. J. de Jonge and M. Bevis (2000). "Instantaneous geodetic positioning at medium distances with the Global Positioning System." <u>Journal of Geophysical Research</u> **105**: 28223-28253.

Borsa, A. A. (2005). Geomorphology of the salar de Uyuni, Bolivia. <u>Scripps Institution of Oceanography</u>. La Jolla, CA, University of California at San Diego.

Chen, G. (1998). GPS kinematic positioning for the airborne laser altimetry at Long Valley, California. <u>Department of Earth, Atmospheric and Planetary Sciences</u>, Massachusetts Institute of Technology.

Dong, D. and Y. Bock (1989). "Global Positioning System network analysis with phase ambiguity resolution applied to crustal deformation studies in California." <u>Journal of Geophysical Research</u> **94**(B4): 3949-3966.

Elósegui, P., J. L. Davis, R. T. K. Jaldehag, J. M. Johansson, A. E. Niell and I. I. Shapiro (1995). "Geodesy using the Global Positioning System: The effects of signal scattering on estimates of site position." <u>Journal of Geophysical Research</u> **100**: 9921-9934.

Genrich, J. F. and Y. Bock (1992). "Rapid resolution of crustal motion at short ranges with the Global Positioning System." <u>Journal of Geophysical Research</u> **97**(B3): 3261-3269.

Genrich, J. F. and Y. Bock (2006). "Instantaneous geodetic positioning with 10-50 Hz GPS measurements: Noise characteristics and implications for monitoring networks." <u>Journal of Geophysical Research</u> **111**(B03403): doi:10.1029/2005JB003617.

Georgiadou, Y. and A. Kleusberg (1988). "On carrier signal multipath effects in relative GPS positioning." <u>Manuscripta Geodaetica</u> **13**: 172-179.

Gutierrez, R., J. C. Gibeaut, R. C. Smyth, T. L. Hepner, J. R. Andrews, C. Weed, W. Gutelius and M. Mastin (2001). "Precise airborne lidar surveying for coastal research and geohazards applications." <u>International Archives of Photogrammetry and Remote Sensing</u> **XXXIV-3/W4**: 185-192.

Herring, T. (2002). Documentation for the TRACK kinematic GPS analysis software, version 1.07. Massachusetts Institute of Technology.

Hofton, M. A., J. B. Blair, J.-B. Minster, J. R. Ridgway, N. P. Williams, J. L. Bufton and D. L. Rabine (2000). "An airborne scanning laser altimetry survey of Long Valley, California." <u>International Journal of Remote Sensing</u> **21**(12): 2413-2437.

Krabill, W. B. and C. F. Martin (1987). "Aircraft positioning using global positioning system carrier phase data." <u>Navigation</u> **34**(1): 1-21.

Krabill, W. B., R. Thomas, K. Jezek, K. Kuivenen and S. Manizade (1995). "Greenland ice sheet thickness changes measured by laser altimetry." Geophysical Research Letters **22**(17): 2341-2344.

Macmillan, D. S. (1995). "Atmospheric gradients from very long baseline interferometry observations." Geophysical Research Letters **22**(9): 1041-1044.

Mader, G. L. (1986). "Dynamic positioning using GPS carrier phase measurements." Manuscripta Geodaetica **11**: 272-277.

Mader, G. L. and J. R. Lucas (1989). "Verification of airborne positioning using Global Positioning System carrier phase measurements." Journal of Geophysical Research **94**(B8): 10175-10181.

Mader, G. L. and J. R. MacKay (1997). Calibration of GPS antennas. 1996 Analysis Center Workshop, International GPS Service Central Bureau, Jet Propulsion Laboratory, Pasadena, California.

Mao, A., C. G. A. Harrison and T. H. Dixon (1999). "Noise in GPS coordinate time series." Journal of Geophysical Research **104**(B2): 2797-2816.

Parker, R. L. (1994). Geophysical Inverse Theory. Princeton, Princeton University Press.

Phillips, H. A., I. Allison, R. Coleman, G. Hyland, P. J. Morgan and N. W. Young (1998). "Comparison of ERS satellite radar altimeter heights with GPS-derived heights on the Amery Ice Shelf, East Antarctica." Annals of Glaciology **27**: 19-24.

Pilgrim, B. and D. T. Kaplan (1998). "A comparison of estimators for 1/f noise." Physica D **114**: 108-122.

Prescott, W. H., J. C. Savage, J. L. Svarc and D. Manaker (2001). "Deformation across the Pacific-North American plate boundary near San Fransisco, California." Journal of Geophysical Research **106**(B4): 6673-6682.

Press, W. H., S. A. Teukolsky, W. T. Vetterling and B. P. Flannery (1992). Numerical Recipes in C. New York, Cambridge University Press.

Ridgway, J. R., J.-B. Minster, N. P. Williams, J. L. Bufton and W. B. Krabill (1997). "Airborne laser altimeter survey of Long Valley, California." Geophysics Journal International **131**: 267-280.

Rowlands, D. D., D. E. Pavlis, F. G. Lemoine, G. A. Neumann and S. B. Luthcke (1999). "The use of laser altimetry in the orbit and attitude determination of Mars Global Surveyor." Geophysical Research Letters **26**: 1191-1194.

Saka, M. H., T. Kavzoglu, C. Ozsamli and R. M. Alkan (2004). "Sub-meter accuracy for stand alone GPS positioning in hydrographic surveying." Journal of Navigation **57**: 135-144.

Williams, S. D. P., Y. Bock, P. Fang, P. Jamason, R. M. Nikolaidis, M. Miller and D. J. Johnson (2004). "Error analysis of continuous GPS positioin time series." Journal of Geophysical Research **109**(B03412): doi:10.1029/2003JB002741.

Zhang, J., Y. Bock, H. Johnson, P. Fang, S. Williams, J. Genrich, S. Wdowinski and J. Behr (1997). "Southern California Permanent GPS Geodetic Array: Error analysis of daily position estimates and site velocities." <u>Journal of Geophysical Research</u> **102**(B8): 18,035-18,055.